

Si-compatible candidates for high- K dielectrics with the $Pbnm$ perovskite structure

Sinisa Coh,^{1,*} Tassilo Heeg,² J. H. Haeni,³ M. D. Biegalski,⁴ J. Lettieri,^{3,†} L. F. Edge,³ K. E. O'Brien,³ M. Bernhagen,⁵ P. Reiche,⁵ R. Uecker,⁵ S. Trolrier-McKinstry,³ Darrell G. Schlom,² and David Vanderbilt¹

¹ *Department of Physics and Astronomy, Rutgers University, Piscataway, NJ 08854-8019, USA*

² *Department of Materials Science and Engineering, Cornell University, Ithaca, NY 14853, USA*

³ *Department of Materials Science and Engineering, Pennsylvania State University, University Park, PA 16802, USA*

⁴ *Center for Nanophase Materials Science, Oak Ridge National Laboratory, Oak Ridge, TN 37830, USA*

⁵ *Leibniz Institute for Crystal Growth, Max-Born-Straße 2, D-12489 Berlin (Adlershof), Germany*

(Dated: October 23, 2018)

We analyze both experimentally (where possible) and theoretically from first-principles the dielectric tensor components and crystal structure of five classes of $Pbnm$ perovskites. All of these materials are believed to be stable on silicon and are therefore promising candidates for high- K dielectrics. We also analyze the structure of these materials with various simple models, decompose the lattice contribution to the dielectric tensor into force constant matrix eigenmode contributions, explore a peculiar correlation between structural and dielectric anisotropies in these compounds and give phonon frequencies and infrared activities of those modes that are infrared-active. We find that CaZrO_3 , SrZrO_3 , LaHoO_3 , and LaYO_3 are among the most promising candidates for high- K dielectrics among the compounds we considered.

PACS numbers: 77.22.-d, 77.55.df, 85.50.-n

I. INTRODUCTION

As a result of the ongoing down-scaling of complementary metal-oxide-semiconductor (CMOS) integrated circuits, the SiO_2 gate oxide of field effect transistors is getting thinner and thinner in every new generation of devices.¹ Therefore the leakage current due to quantum-mechanical tunneling through the dielectric interface is increasing. One way to reduce this current is to replace SiO_2 with a material that has a higher dielectric constant. Such a high- K dielectric layer with the same effective dielectric thickness (i.e., providing the same capacitance) could be physically thicker and thus reduce the gate leakage.

In order for this replacement material to be useful in practical applications on silicon, it also needs to be stable in contact with silicon up to ~ 1000 °C, and among other things it must also have an appropriate band alignment with silicon.²⁻⁴ Currently, a hafnia-based dielectric is used as a replacement to SiO_2 in advanced CMOS transistors in production.⁵⁻⁷ There are, however, drawbacks to this material too, e.g., the limited K that it provides and undesirable threshold voltage shifts arising from highly mobile oxygen vacancies.⁸ This brings up the natural question: *which other materials exist that would satisfy these requirements and would enable the scaling of MOSFETs to continue beyond today's hafnia-based dielectrics?*

The stability of single component oxides on silicon has been demonstrated both experimentally and from thermodynamic analysis,³ and a candidate list of multicomponent oxide materials has been compiled.² A promising group of these materials consists of perovskite oxides having a $Pbnm$ (or closely related $P2_1/c$) space group. These compounds are at the focus of the present work. Some

of them have been studied in thin-film form,⁹⁻²⁷ but the full dielectric tensor of these materials has not yet been established, making the selection of materials best suited for high- K applications difficult. Some of these materials could also be of interest for microwave dielectric applications.^{28,29} Thus we decided to study, both theoretically and experimentally, the structural and dielectric properties of these compounds. The calculations are carried out using density-functional theory, and we compare the results with experimental data where we could obtain suitable samples for measurements. To our knowledge, previous theoretical calculations have been carried out in only a few cases.³⁰⁻³²

The paper is organized as follows. Explanations of both the experimental and theoretical methods used in this work are given in Sec. II. The main results on the structural and dielectric properties are given and discussed in Sec. III. There we also discuss the correlations between the structural and dielectric properties of these perovskites, decompose the ionic contribution of the dielectric tensor into components arising from various force constant matrix eigenvectors, and discuss the effect of B_A antisite defects on the dielectric properties. We finish with a brief summary in Sec. IV.

Supplementary material³³ contains the results of our calculations of the zone-center phonon frequencies, as well as the infrared activities for those modes that are infrared-active.

A. Compounds under consideration

In this work, we consider the following five groups of perovskites having the $Pbnm$ space group.

The first group are rare-earth scandates having for-



FIG. 1: Photographs of single crystal rare-earth scandates grown along the $[110]$ direction by the Czochralski method. (a) PrScO_3 with a diameter of 12 mm, (b) NdScO_3 with a diameter of 16 mm, (c) SmScO_3 with a diameter of 18 mm, (d) GdScO_3 with a diameter of 32 mm, (e) TbScO_3 with a diameter of 18 mm, and (f) DyScO_3 with a diameter of 32 mm.

mula $A\text{ScO}_3$ where A is a rare-earth atom. In Sec. III C 1 we report experimental measurements of the full dielectric tensors for PrScO_3 , NdScO_3 , SmScO_3 , GdScO_3 and DyScO_3 . Calculations were done on these and also on LaScO_3 and TbScO_3 . Note that HoScO_3 , ErScO_3 , TmScO_3 , YbScO_3 , LuScO_3 , and YScO_3 do not form single crystals with the perovskite structure from the melt at atmospheric pressure. Rather, they form solid solutions of $A_2\text{O}_3$ and Sc_2O_3 , i.e., $(A,\text{Sc})_2\text{O}_3$, with the bixbyite structure.^{34–36} Nevertheless, LuScO_3 ²⁷ and YbScO_3 ³⁷ have been formed in perovskite form as thin films via epitaxial stabilization, and others might be made in the same way. To analyze trends within this group of compounds, we also did the calculations of dielectric tensors on LuScO_3 and YScO_3 in the $Pbnm$ perovskite structure; see Sec. III C 1 for the details.

The second group consists of rare-earth yttrates with formula $A\text{YO}_3$. Only one such compound, LaYO_3 , is known to form a perovskite,³⁸ but to analyze trends the dielectric tensor of DyYO_3 in the perovskite structure was also calculated.

In the third group we consider CaZrO_3 , SrZrO_3 and SrHfO_3 perovskites. Experimentally, we find that SrZrO_3 and SrHfO_3 do not form single crystals, but instead are rather heavily twinned.

The fourth group of compounds have the formula $\text{La}_2B\text{B}'\text{O}_6$ where the B atom is either Mg or Ca and B' is either Zr or Hf. Little is known experimentally about these compounds, and single crystals of these compounds have not been made.³⁹

The last group of compounds we considered have the formula $AA'\text{O}_3$, where both A and A' are rare-earth atoms. These include the 11 of such compounds that are known to form the perovskite structure with space group $Pbnm$ at atmospheric pressure: LaHoO_3 , LaErO_3 , LaTmO_3 , LaYbO_3 , LaLuO_3 , CeTmO_3 , CeYbO_3 , CeLuO_3 , PrYbO_3 , PrLuO_3 , and NdLuO_3 .^{38,40,41} We calculated the dielectric and structural properties of all of these compounds. The experimental determination, however, of the dielectric tensor in this group of compounds was done only for LaLuO_3 ; the results will be published elsewhere.⁴²

II. PRELIMINARIES

A. Structure of $Pbnm$ perovskites

The ideal cubic perovskite ABO_3 consists of a network of corner-shared octahedra, each with an oxygen on its vertices and a B atom at its center, and A ions that are 12-fold coordinated in the spaces between octahedra. It is well known that perovskites having sufficiently small A -site ions (i.e., a small Goldschmidt tolerance factor^{43,44}) often allow for a distorted perovskite structure that has a rotated framework of oxygen octahedra and displaced A -site ions. This lowers the space group symmetry from cubic $Pm\bar{3}m$ (O_h^1) to orthorhombic $Pbnm$ (D_{2h}^{16}), and the number of ABO_3 formula units per primitive cell increases from $Z = 1$ to $Z = 4$, as shown in Fig. 2. The rotations of the octahedra in the $Pbnm$ space group can be decomposed into two steps. The first step is the rotation around the $[110]$ direction of the original cubic frame (the cubic frame is rotated by 45° around the z axis with respect to the $Pbnm$ frame) by an angle θ_R as in Fig. 3(a), and the second step is a rotation around $[001]$ by θ_M as in Fig. 3(b). The rotations must be done in that order to prevent distortions of the octahedra. The pattern of neighboring octahedral rotations is denoted by $(a^-a^-c^+)$ in Glazer notation⁴⁵ (or see the directions of the arrows in Fig. 3). These rotations also allow for the displacement of A -site ions in the x - y plane without further lowering of the space-group symmetry.

B. Computational methods

The main computational method we are using is the density-functional theory as implemented in the Quantum-Espresso package.⁴⁶ The exchange-correlation functional was approximated using a generalized gradient approximation (GGA) of the Perdew-Burke-Ernzerhof type⁴⁷ and ultrasoft pseudopotentials were employed.⁴⁸ The electronic wavefunctions were expanded in a basis of plane waves with kinetic energy up to 40 Ry, while the charge density was expanded up to 300 Ry. The Brillouin zone was sampled using a $4 \times 4 \times 4$ Monkhorst-Pack grid.⁴⁹

A new set of ultrasoft pseudopotentials⁴⁸ for the lanthanoid series of rare earths, from La to Lu, were generated for the present project. In all cases the f -shell filling was chosen as appropriate for the 3+ valence state: one f electron for Ce, two for Pr, etc. The f electrons were then

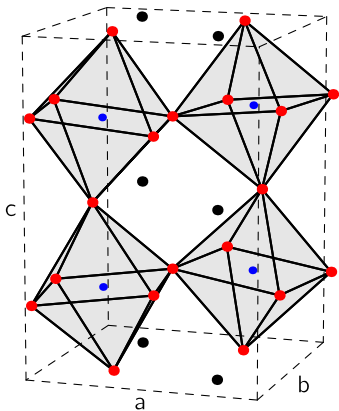


FIG. 2: (Color online) 20-atom primitive cell of a $Pbnm$ -distorted ABO_3 perovskite. A -site atoms are shown in black, B -site atoms in blue (at the centers of the octahedra) and oxygen atoms in red (at the vertices of the octahedra). Orthorhombic unit cell vectors (a , b , and c) are also indicated.

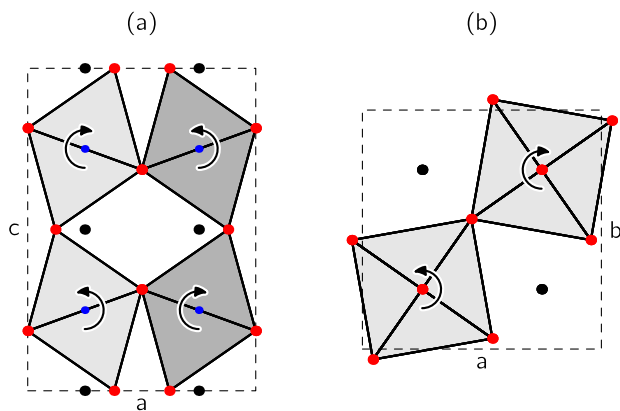


FIG. 3: (Color online) (a) Projection on the a - c plane of the structure with $\theta_R > 0$ and $\theta_M = 0$. (b) Projection on the a - b plane for $\theta_R = 0$ and $\theta_M > 0$. Color coding of atoms and positions of axes labels are the same as in Fig. 2. In (a), a darker shading is used to indicate the two octahedra that are further away along the y -coordinate; in (b), the two bottom octahedra are exactly below the two top octahedra.

considered to be in the core (and un-spin-polarized) for the purposes of generating the pseudopotentials. Thus, the f electrons are not explicitly included in the solid-state calculations. Such an approximation can be justified whenever the strong on-site Coulomb interactions of electrons in the f shell drive the occupied f states well below, and the unoccupied states well above, the energy range of interest for spd bonding in the crystal. Of course, this will not be a good approximation for some heavy-fermion or mixed-valent systems, and in any case our approach is obviously unable to describe phenomena involving magnetic ordering of f electrons at low temperature. Nevertheless, we believe that this approach is quite reasonable for the present purposes.

The artificial nature of the scattering in the f channel

did, however, pose some problems in the pseudopotential construction. In particular, we found that the lattice constant of a perovskite containing the rare-earth atom in question could differ for two pseudopotentials having different scattering properties in the f channel; this causes problems since the usual approach of matching to the all-electron f scattering is not appropriate in the present case. To ameliorate this problem, the f -channel parameters of these pseudopotentials were optimized so that resulting pseudopotentials would give the “correct” cell volumes for simple rare-earth compounds. Since the GGA typically overestimates crystal volumes by about 1-2%,⁵⁰ the optimization was actually done in order to produce a corresponding overestimate in a consistent fashion.

For this procedure, our compounds of choice were the rare-earth nitrides with the simple rock-salt structure. The experimental⁵¹ and calculated volumes of these nitrides are indicated in Fig. 4. Note that the volumes of CeN, PrN, and GdN show an anomalous behavior that is presumably due to strong correlation effects associated with the proximity to a mixed-valent regime,⁵² and therefore they will not be correctly treated by our GGA calculation. To avoid this problem we first carried out a smoothed fit of the experimental volumes versus atomic number over the lanthanide nitride series, but with CeN, PrN, and GdN omitted from the fit, as shown by the solid line in Fig. 4. We then used these fitted values to set the target volumes for the optimization of the pseudopotentials.

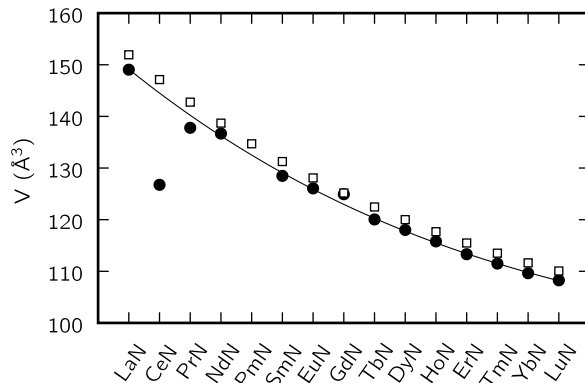


FIG. 4: Unit cell volumes of all rock-salt rare-earth nitrides, in \AA^3 . Empty squares are the results obtained using our optimized ultrasoft pseudopotentials for rare-earth atoms; solid circles are experimental⁵¹ results. The solid line is a fit to the experimental values excluding CeN, PrN, and GdN.

We used density-functional perturbation theory⁵³ to calculate the dielectric response. Both purely electronic ϵ^{el} and ionic ϵ^{ion} contributions were calculated.⁵⁴ The electronic part is defined as

$$\epsilon_{\alpha\beta}^{\text{el}} = \delta_{\alpha\beta} + 4\pi \left. \frac{\partial P_\alpha}{\partial \mathcal{E}_\beta} \right|_{u=0}, \quad (1)$$

where P_α is the polarization induced by the electric field

\mathcal{E}_β while all ions are held fixed ($u = 0$). The remaining component of the dielectric response is by definition the ionic contribution ϵ^{ion} .

This ionic part can be calculated from the force-constant matrix $\Phi_{i\alpha,j\beta}$ and the Born effective charge matrix $Z_{i,\alpha\beta}$. The force-constant matrix is defined as

$$\Phi_{i\alpha,j\beta} = \frac{\partial^2 E}{\partial u_{i\alpha} \partial u_{j\beta}}, \quad (2)$$

where E is the total energy of the system and $u_{i\alpha}$ is the displacement of the i -th atom along the direction α . We will denote the n -th normalized eigenvector of this matrix as $\xi_{i\alpha}^n$ and its eigenvalue as μ_n . The Born effective charge matrix is defined as

$$Z_{i,\alpha\beta} = \frac{V}{e} \frac{\partial P_\alpha}{\partial u_{i\beta}}, \quad (3)$$

where P_α is the polarization induced in a crystal by the displacement of the i -th atom in the direction β . V is the volume of the unit cell and e is the electron charge. Finally, the ionic part of the dielectric tensor can be written as

$$\epsilon_{\alpha\beta}^{\text{ion}} = \frac{4\pi e^2}{V} \sum_n \frac{1}{\mu_n} Q_\alpha^n Q_\beta^n, \quad (4)$$

where the charge Q_α^n of the n -th eigenmode is defined through the effective charge matrix as $Q_\alpha^n = \sum_{i\beta} Z_{i,\alpha\beta} \xi_{i\beta}^n$.

C. Experimental methods

1. Crystal growth

PrScO₃, NdScO₃, SmScO₃, GdScO₃, TbScO₃, and DyScO₃ single crystals were grown using an automated Czochralski technique with RF-induction heating.^{55,56} Pre-dried powders of Sc₂O₃, Pr₆O₁₁, Nd₂O₃, Sm₂O₃, Gd₂O₃, Tb₄O₇, and Dy₂O₃, were mixed in the stoichiometric ratio, pressed, and sintered at about 1400 °C for 15 h. Due to the high melting temperature of PrScO₃, NdScO₃, SmScO₃, GdScO₃, TbScO₃, and DyScO₃ (~2100 °C), a crucible (cylindrical with 40 mm or 60 mm diameter and 40 mm or 60 mm height, depending on the crystal diameter) and an active afterheater made of iridium were used. Flowing nitrogen or argon was used as the growth atmosphere. Those of these rare-earth scandates for which the radiative heat transport via the crystal is hindered by absorption suffer from a serious problem of bulk crystal growth, namely that they tend to exhibit a spiral growth which distinctly decreases the yield.⁵⁵ Due to the lack of seed crystals, the initial growth experiments were performed with an iridium seed rod. Because these materials tend to grow as large single-crystalline grains, suitable seeds could be selected at a very early stage.

All rare-earth scandate crystals were grown along the [110] orientation. The pulling rate was 0.8-2 mm·h⁻¹ and the rotation rate was 8-15 min⁻¹ (depending on the crystal diameter). The crystals were 35-50 mm in length and 18 or 32 mm in diameter. The PrScO₃ crystals have a green color, the NdScO₃ crystals are dark purple, the SmScO₃ and DyScO₃ crystals are light yellow, the GdScO₃ crystals are colorless, and the TbScO₃ crystals are nearly colorless (see Fig. 1).

In addition to the Czochralski growth of PrScO₃, NdScO₃, SmScO₃, GdScO₃, TbScO₃, and DyScO₃, the single-crystal growth of HoScO₃, YScO₃, and solid solutions of rare-earth scandates that would be expected to have smaller lattice constants than DyScO₃ (e.g., Dy_{0.5}Lu_{0.5}ScO₃), was also attempted using the floating-zone technique. In all cases, pre-dried powders of the rare-earth oxides (R_2O_3) and Sc₂O₃ were ground, pressed into a rod, and sintered at 1400 °C for 6 hours. The floating-zone machine was a Gero (model SPO), and heating was performed with two bulbs at the focal point of ellipsoidal mirrors. Unfortunately, the 1 kW rated output power of the quartz-halogen lamps used in this floating-zone system was close to the melting temperature of the compounds, limiting the size of the crystals that could be grown to < 2 mm diameter. SrZrO₃, SrHfO₃, and LaScO₃ single crystals grown by the floating zone technique were also studied.⁵⁷

The available R_2O_3 -Sc₂O₃ binary phase diagrams show a distinct transition between the Dy₂O₃-Sc₂O₃ and the Ho₂O₃-Sc₂O₃ systems (Dy and Ho are neighboring elements in the periodic table). According to published phase diagrams, the rare-earth elements of La, Nd, Sm, Gd, and Dy all form $RScO_3$ compounds that melt congruently. In contrast the oxides of Ho, Er, Tm, Yb, and Lu form complete solid solutions with Sc₂O₃ at their melting points.³⁴⁻³⁶ (The same happens with Y as well.³⁴⁻³⁶) Although HoScO₃ has been synthesized with solid-state techniques at temperatures (well below the melting point) at which the perovskite polymorph of HoScO₃ is stable, our results confirm that the perovskite polymorph of HoScO₃ is not stable at its melting point in agreement with existing phase diagrams. Analysis of our Y-Sc-O and Ho-Sc-O single crystals revealed that they were solid solution mixtures of Ho₂O₃ and Sc₂O₃, and Y₂O₃ and Sc₂O₃, not the desired perovskite polymorphs of HoScO₃ and YScO₃. The only compound that did not behave according to its phase diagram was LaScO₃. Attempts to grow LaScO₃ resulted in crystals that were a mixture of three different phases including LaScO₃, Sc₂O₃, and a third, unidentified phase.⁵⁷ X-ray analysis of the post-annealed polycrystalline feed rod showed single-phase LaScO₃, consistent with the existing phase diagram. The reason for the introduction of second phases during melting is not clear and requires more study.

2. Electrical characterization

Because PrScO_3 , NdScO_3 , SmScO_3 , GdScO_3 , and DyScO_3 are orthorhombic at room temperature, their dielectric tensor contains three independent coefficients that can be measured along the three principle crystal axes.⁵⁸ From the grown PrScO_3 , NdScO_3 , SmScO_3 , GdScO_3 , and DyScO_3 single crystals, slices were cut in different orientations for electrical characterization. For GdScO_3 , samples were cut from the as-grown single crystals along the [100], [010], and [001] directions, and the dielectric tensor coefficients were measured using a parallel-plate capacitor configuration. For PrScO_3 , NdScO_3 , SmScO_3 , and DyScO_3 , several additional orientations were prepared, so that a least-squares fit technique could be applied using standard methods⁵⁸ to calculate the dielectric tensor, using their known lattice parameters.^{56,59}

Unfortunately, the SrZrO_3 and SrHfO_3 crystals were heavily twinned. The formation of twins in the three pseudocubic orientations is facilitated in these two orthorhombic systems because the deviation from the cubic symmetry is very small. As a result, only an average dielectric constant could be measured.

To obtain capacitors, gold or platinum electrodes were evaporated onto both sides of the approximately 0.5 mm thick slabs with areas ranging from 15 to 100 mm², and capacitance measurements were made at room temperature with an HP4284A using a 16034E test fixture at 10 kHz, 100 kHz, and 1 MHz. No edge capacitance corrections were used because of the large ratio of the electrode area to the thickness of the samples. The room temperature dielectric loss of the samples was generally very small (< 0.1% for most samples) and the frequency dispersion was negligible in the measured range. The temperature dependent dielectric measurements on GdScO_3 and DyScO_3 were made using a HP 4284a LCR meter with a dipstick cryostat.

III. RESULTS AND DISCUSSION

A. Structural properties

We focus first on the structural properties of these systems. The structure of the $Pbnm$ perovskites is described by three orthorhombic lattice constants plus two A -site and five oxygen Wyckoff parameters. Figure 5 shows graphically the most important structural parameters of these systems, while Table I gives detailed information on all the structural parameters. Rotational angles in Table I and in Fig. 5 were calculated by fitting the structural parameters to a model in which the octahedra are perfectly rigid (see Sec. III B for the details of this model).

Overall we find good agreement with experimental values for the structural parameters. The Wyckoff coordinates in particular are in excellent agreement with experiments, with the average error being on the order of

$2 \cdot 10^{-3}$. The volume of the unit cell, on the other hand, is consistently overestimated by 1-2%, as is usually expected from the GGA exchange-correlation functional, and as we would expect from our construction of the rare-earth pseudopotentials.

All structures show an angle θ_R that is about $\sqrt{2}$ times larger than θ_M . Therefore, consecutive rotations by θ_R and θ_M can be considered approximately as a single rotation around a {111} axis in the cubic frame. That is, the actual ($a^- a^- c^+$) pattern of rotations is very nearly ($a^- a^- a^+$) in the Glazer notation.⁴⁵ See Sec. III F for a more detailed discussion.

1. Rare-earth scandates

The rare-earth scandates $A\text{ScO}_3$ show a decrease in volume by $\sim 9\%$ while going along the series from $A=\text{La}$ to $A=\text{Dy}$ (the calculated primitive unit cell volume is 271.40 Å³ for LaScO_3 and 249.81 Å³ for DyScO_3). On the other hand, the Sc-O distance remains nearly constant along the series (2.12 Å for LaScO_3 and 2.11 Å for DyScO_3), which means that the change in volume is almost entirely due to the larger octahedral rotation angles for DyScO_3 as compared to LaScO_3 . Our calculations also show that the same trend continues all the way to LuScO_3 .

2. Rare-earth yttrates

The rare-earth yttrates have a very similar behavior as the rare-earth scandates. The main quantitative structural difference between the two comes from the fact that yttrium is a larger ion than scandium. This leads to a larger volume for the yttrates, and also a larger rotation angle due to a smaller tolerance factor.

3. CaZrO_3 , SrZrO_3 , and SrHfO_3

SrZrO_3 and SrHfO_3 have quite similar structural properties. The main difference can be traced to the fact that Hf is a smaller ion than Zr. Therefore, the calculated average Hf-O distance is 2.07 Å, while the average Zr-O distance is 2.11 Å. Furthermore, their octahedral rotation angles are about 1.7 times smaller than in the rare-earth scandates.

In CaZrO_3 the average Zr-O distance is 2.10 Å, which is very close to the corresponding distance in SrZrO_3 and SrHfO_3 . Thus, the main reason why CaZrO_3 has a smaller volume than SrZrO_3 is because of the larger rotation angles in CaZrO_3 .

4. $\text{La}_2\text{BB}'\text{O}_6$ compounds

We consider $\text{La}_2\text{BB}'\text{O}_6$ compounds with $B=\text{Mg}$ or Ca and $B'=\text{Zr}$ or Hf . These compounds are expected to exhibit rock-salt ordering of the B -site ions as a result of the difference in charge and ionic radius between the B and B' ions.⁶⁰ This ordering reduces the symmetry from the orthorhombic $Pbnm$ to the monoclinic $P2_1/c$ (C_{2h}^5) space group.

The structural properties for these systems are reported in Fig. 5 and in Table II. The rotational angles are obtained by a fit to the rigid-octahedra model in which we have allowed for different sizes of B - and B' -centered octahedra. (See the end of Sec. III B for details.)

The unit cell volume is larger by about 5 \AA^3 per primitive cell for the compounds containing Zr than for those containing Hf . On the other hand, compounds with Ca are larger by about 28 \AA^3 than those containing Mg . Similarly, the rotation angles are larger in compounds containing Ca than in those with Mg . The discrepancy between octahedral sizes is largest for $\text{La}_2\text{CaHfO}_6$ (12% linear increase) and smallest for $\text{La}_2\text{MgZrO}_6$ (0.4% linear increase).

5. Rare-earth rare-earth perovskites

We now briefly analyze the structural properties of $Pbnm$ perovskites of type $AA'\text{O}_3$ where both A and A' are rare-earth atoms. All eleven compounds we considered are known experimentally to form the perovskite structure in the $Pbnm$ space group.^{38,40,41}

Among these 11 compounds, the largest unit-cell volume of 311.58 \AA^3 is found in LaHoO_3 , and the smallest of 292.32 \AA^3 is in NdLuO_3 . Oxygen octahedral rotation angles are quite large in all of these compounds and show very little variation from one compound to another. The trends of the rotation angles are as expected from a tolerance-factor analysis: perovskites with smaller A -site ions but the same B -site ions have larger oxygen octahedral rotation angles, and the opposite is true for the B -site ions.

B. Comparison with model of perfectly rigid octahedra

In $Pbnm$ perovskites, a rigid rotation of the oxygen octahedra by θ_R followed by another rigid rotation by

θ_M (see Fig. 3) leads to Wyckoff parameters given by

$$x_2 = -\frac{1}{2\sqrt{2}} \tan \theta_R, \quad (5)$$

$$y_2 = -\frac{1}{2\sqrt{2}} \sin \theta_R \tan \theta_M, \quad (6)$$

$$x_3 = \frac{1}{4} \left(1 - \frac{\tan \theta_M}{\cos \theta_R} \right), \quad (7)$$

$$y_3 = \frac{1}{4} (1 + \cos \theta_R \tan \theta_M), \quad (8)$$

$$z_3 = \frac{1}{4\sqrt{2}} \tan \theta_R, \quad (9)$$

Here we have denoted the Wyckoff coordinates of the oxygen atoms at the $4c$ Wyckoff point with x_2 and y_2 , while those of the remaining oxygen atoms at the $8d$ point are denoted with x_3 , y_3 , and z_3 . The Wyckoff coordinates of the A -site ion at the $4c$ point are denoted by x_1 and y_1 , but these are left unspecified in our rigid-octahedra model. It also leads to orthorhombic lattice constants given by

$$a = \sqrt[3]{\frac{V_0}{\sqrt{2}}} \cos \theta_R \cos \theta_M, \quad (10)$$

$$b = \sqrt[3]{\frac{V_0}{\sqrt{2}}} \cos \theta_M, \quad (11)$$

$$c = \sqrt[3]{2V_0} \cos \theta_R \quad (12)$$

where V_0 is the volume the structure would have if the octahedra were rotated rigidly back to $\theta_R = \theta_M = 0$.

The Wyckoff parameters and unit-cell ratios from our calculations can be well fitted by Eqs. 5-12 (see Table I and Fig. 5 for the values of the fitted angles). By far the largest discrepancy is found for Wyckoff parameter y_2 . For a typical system (e.g., LaScO_3) the discrepancy between calculated and fitted y_2 values is about 0.016, or 50% with respect to the difference from the cubic case. For the remaining oxygen Wyckoff coefficients, the discrepancy averages about 0.003, or $\sim 5\%$.

The rotation angles for the $\text{La}_2\text{BB}'\text{O}_6$ systems were obtained by fitting their structural parameters to a slightly more complicated model of rigid octahedra than the one given in Eqs. 5-12. In this model, we first change the relative sizes of B - and B' -centered octahedra. The ratio of their linear sizes is denoted by d/d' . We then proceed with the rotation by an angle θ_R around the $[110]$ axis in the cubic frame. Finally, we perform a rotation of the B -centered octahedra around $[001]$ by an angle θ_M , and of the B' -centered octahedra by an angle θ'_M around the same axis. The resulting fitted values of these parameters are given in Table II.

C. Dielectric properties

In this section we discuss the dielectric properties of the materials included in our study. $Pbnm$ perovskites are

TABLE I: Structural parameters of the $Pbnm$ perovskites we considered. Our calculated values are indicated with the letter T, experimental values with E and other theoretical data with O. Fitted octahedra rotation angles θ_R and θ_M are given in degrees, see Sec. III B for the details. A -site ions occupy the $4c$ site and in cubic configuration $x_1 = 0$ and $y_1 = 1/2$. B -site ions are on the $4a$ site. One type of oxygen sites are at $4c$ and in the cubic case $x_2 = 0$ and $y_2 = 0$. The remaining oxygens are at $8d$ and $x_3 = 1/4$, $y_3 = 1/4$ and $z_3 = 0$ in the cubic case.

		Unit cell parameters						Wyckoff coordinates						Model		
		a (Å)	b (Å)	c (Å)	V (Å ³)	b/a	c/a	x_1	y_1	x_2	y_2	x_3	y_3	z_3	θ_R (°)	θ_M (°)
LaScO ₃	T	5.7030	5.8414	8.1469	271.40	1.0243	1.4285	0.0123	0.5467	-0.0977	-0.0323	0.2059	0.2943	0.0523	14.9	9.9
	E ^a	5.6803	5.7907	8.0945	266.25	1.0194	1.4250	0.0100	0.5428	-0.0968	-0.0277	0.2073	0.2958	0.0521	14.6	9.6
PrScO ₃	T	5.6372	5.8367	8.0908	266.21	1.0354	1.4352	0.0148	0.5537	-0.1049	-0.0377	0.2014	0.2979	0.0557	16.4	11.0
	E ^j	5.608	5.780	8.025	260.1	1.0307	1.4310	0.0121	0.5507	-0.1052	-0.0395	0.1977	0.3008	0.0555	16.2	11.2
NdScO ₃	T	5.6077	5.8317	8.0667	263.80	1.0399	1.4385	0.0159	0.5562	-0.1083	-0.0401	0.1997	0.2992	0.0574	17.0	11.5
	E ^b	5.577	5.777	8.005	257.9	1.0359	1.4354	0.0133	0.5532	-0.1088	-0.0418	0.1953	0.3020	0.0571	16.8	11.8
SmScO ₃	T	5.5483	5.8067	8.0196	258.37	1.0466	1.4454	0.0176	0.5596	-0.1159	-0.0455	0.1964	0.3019	0.0610	18.2	12.5
	E ^b	5.531	5.758	7.975	254.0	1.0410	1.4419	0.0149	0.5566	-0.1163	-0.0468	0.1935	0.3037	0.0609	17.9	12.5
GdScO ₃	T	5.4987	5.7794	7.9861	253.79	1.0510	1.4524	0.0191	0.5617	-0.1222	-0.0502	0.1941	0.3036	0.0642	19.0	13.3
	E ^b	5.481	5.745	7.929	249.7	1.0482	1.4466	0.0163	0.5599	-0.1209	-0.0501	0.1912	0.3052	0.0628	18.7	13.2
TbScO ₃	T	5.4764	5.7646	7.9735	251.72	1.0526	1.4560	0.0198	0.5624	-0.1251	-0.0524	0.1932	0.3043	0.0656	19.4	13.7
	E ^k	5.4543	5.7233	7.9147	247.07	1.0493	1.4511	0.0167	0.5603	-0.1239	-0.0545	0.1900	0.3054	0.0643	19.1	13.7
DyScO ₃	T	5.4560	5.7501	7.9629	249.81	1.0539	1.4595	0.0203	0.5630	-0.1276	-0.0545	0.1923	0.3050	0.0669	19.7	14.1
	O ^f	5.449	5.739	7.929	248.0	1.0532	1.4551	0.019	0.562	-0.130	-0.057	0.190	0.307	0.068	19.9	14.1
LaYO ₃	E ^b	5.443	5.717	7.901	245.9	1.0503	1.4516	0.0174	0.5616	-0.1262	-0.0561	0.1886	0.3063	0.0659	19.4	13.9
	T	5.9035	6.1225	8.5810	310.16	1.0371	1.4535	0.0173	0.5506	-0.1284	-0.0581	0.1948	0.3035	0.0689	18.9	13.6
CaZrO ₃	E ^l	5.890	6.086	8.511	305.1	1.0333	1.4450									
	T	5.5974	5.7875	8.0416	260.51	1.0340	1.4367	0.0133	0.5506	-0.1078	-0.0413	0.1976	0.2999	0.0572	16.6	11.6
SrZrO ₃	E ^m	5.5831	5.7590	8.0070	257.45	1.0315	1.4341	0.0122	0.5495	-0.1044	-0.0401	0.1976	0.3000	0.0554	16.2	11.4
	T	5.8068	5.8602	8.2323	280.14	1.0092	1.4177	0.0070	0.5311	-0.0759	-0.0195	0.2140	0.2857	0.0401	11.6	7.7
SrHfO ₃	O ^g	5.652	5.664	7.995	255.9	1.0021	1.4145	0.007	0.534	-0.107	-0.036	0.199	0.301	0.056	14.7	10.0
	E ^c	5.7963	5.8171	8.2048	276.65	1.0036	1.4155	0.0040	0.5242	-0.0687	-0.0133	0.2154	0.2837	0.0363	10.4	7.2
	T	5.7552	5.7754	8.1365	270.45	1.0035	1.4138	0.0052	0.5230	-0.0660	-0.0128	0.2209	0.2792	0.0346	10.0	6.2
LaHoO ₃	O ^h	5.6887	5.7016	8.0455	260.95	1.0023	1.4143	0.006	0.528	-0.073	-0.016	0.2166	0.2834	0.0385	10.8	7.0
	E ^d	5.7516	5.7646	8.1344	269.70	1.0023	1.4143	0.0040	0.5160	-0.0630	-0.0140	0.2189	0.2789	0.0335	9.6	6.4
	T	5.9135	6.1367	8.5859	311.58	1.0377	1.4519	0.0170	0.5508	-0.1293	-0.0587	0.1936	0.3044	0.0692	19.0	13.6
LaErO ₃	E ⁱ	5.884	6.094	8.508	305.1	1.0357	1.4460									
	T	5.8971	6.1174	8.5509	308.48	1.0374	1.4500	0.0169	0.5509	-0.1272	-0.0567	0.1945	0.3036	0.0681	18.7	13.3
LaTmO ₃	E ⁱ	5.870	6.073	8.465	301.8	1.0346	1.4421									
	T	5.8829	6.1002	8.5190	305.73	1.0369	1.4481	0.0167	0.5509	-0.1252	-0.0549	0.1951	0.3030	0.0670	18.5	13.1
LaYbO ₃	E ⁱ	5.859	6.047	8.453	299.5	1.0321	1.4427									
	T	5.8692	6.0833	8.4890	303.09	1.0365	1.4464	0.0164	0.5509	-0.1233	-0.0532	0.1957	0.3024	0.0659	18.3	12.8
LaLuO ₃	E ⁱ	5.843	6.033	8.432	297.2	1.0325	1.4431									
	T	5.8579	6.0695	8.4646	300.95	1.0361	1.4450	0.0162	0.5508	-0.1217	-0.0518	0.1962	0.3020	0.0651	18.2	12.6
CeTmO ₃	E ^e	5.8259	6.0218	8.3804	294.00	1.0336	1.4385	0.0138	0.5507	-0.121	-0.056	0.193	0.307	0.063	17.9	12.7
	T	5.8520	6.0870	8.4984	302.72	1.0401	1.4522	0.0179	0.5528	-0.1283	-0.0575	0.1942	0.3036	0.0686	19.0	13.5
CeYbO ₃	E ⁱ	5.828	6.035	8.405	295.6	1.0355	1.4422									
	T	5.8381	6.0707	8.4671	300.09	1.0398	1.4503	0.0176	0.5529	-0.1264	-0.0558	0.1948	0.3031	0.0676	18.8	13.3
CeLuO ₃	E ⁱ	5.806	6.009	8.373	292.1	1.0350	1.4421									
	T	5.8270	6.0578	8.4420	297.99	1.0396	1.4488	0.0174	0.5529	-0.1249	-0.0544	0.1952	0.3027	0.0667	18.7	13.1
PrYbO ₃	E ⁱ	5.793	5.997	8.344	289.9	1.0352	1.4404									
	T	5.8085	6.0544	8.4481	297.10	1.0423	1.4544	0.0185	0.5542	-0.1296	-0.0585	0.1936	0.3039	0.0692	19.3	13.7
PrLuO ₃	E ⁱ	5.776	5.995	8.368	289.8	1.0379	1.4488									
	T	5.7974	6.0424	8.4217	295.01	1.0423	1.4527	0.0183	0.5543	-0.1281	-0.0571	0.1936	0.3036	0.0683	19.1	13.5
NdLuO ₃	E ⁱ	5.768	5.991	8.340	288.2	1.0387	1.4459									
	T	5.7699	6.0270	8.4062	292.32	1.0446	1.4569	0.0193	0.5555	-0.1310	-0.0596	0.1932	0.3042	0.0699	19.5	14.0
	E ⁱ	5.737	5.974	8.311	284.8	1.0413	1.4487									

^a Reference [61]. ^b Reference [62]. ^c Reference [63]. ^d Reference [64]. ^e Reference [40]. ^f Reference [30]. ^g Reference [31]. ^h Reference [32]. ⁱ Reference [38]. ^j Reference [59]. ^k Reference [65]. ^l Reference [66]. ^m Reference [67].

TABLE II: Structural parameters of the $\text{La}_2\text{BB}'\text{O}_6$ perovskites we considered, space group $P2_1/c$. Angles are given in degrees, unit cell vectors in \AA and unit cell volumes in \AA^3 . Monoclinic angle between a and c lattice vectors is denoted as α_{ac} . A -site ions occupy the $4e$ site with coordinate $(3/4, 1/2, 1/4)$. B -site ions (either Mg or Ca) occupy the $2a$ site and B' (Zr or Hf) occupy the $2d$ site. There are three non-equivalent positions for oxygens and they all occupy $4e$ sites. Coordinates of oxygen atoms in the cubic case are $(1/2, 0, 1/4)$, $(1/4, 1/4, 0)$, and $(3/4, 1/4, 0)$. Fitting parameters θ_R , θ_M , θ'_M and d/d' are also given; see Sec. III B for the details.

	Unit cell		Model		Wyckoff coordinates			
	a	b	θ_R	θ_M	La	x	y	z
$\text{La}_2\text{MgZrO}_6$	a	5.6899	θ_R	15.7	O _I	0.7634	0.4546	0.2489
	b	5.8169	θ_M	10.0	O _{II}	0.6538	0.0305	0.2505
	c	8.1274	θ'_M	10.1	O _{III}	0.2411	0.2080	0.0523
	α_{ac}	90.301	d/d'	1.004		0.8429	0.2938	-0.0499
	V	269.00						
$\text{La}_2\text{MgHfO}_6$	a	5.6669	θ_R	14.9	La	0.7622	0.4578	0.2490
	b	5.7679	θ_M	9.3	O _I	0.6567	0.0270	0.2525
	c	8.0765	θ'_M	9.5	O _{II}	0.2430	0.2121	0.0498
	α_{ac}	90.205	d/d'	1.018	O _{III}	0.8356	0.2928	-0.0474
	V	263.99						
$\text{La}_2\text{CaZrO}_6$	a	5.8188	θ_R	19.9	La	0.7698	0.4469	0.2471
	b	6.0547	θ_M	12.0	O _I	0.6134	0.0538	0.2649
	c	8.4245	θ'_M	13.2	O _{II}	0.2464	0.2123	0.0708
	α_{ac}	90.182	d/d'	1.100	O _{III}	0.8500	0.3142	-0.0588
	V	296.80						
$\text{La}_2\text{CaHfO}_6$	a	5.7946	θ_R	19.3	La	0.7687	0.4477	0.2474
	b	6.0211	θ_M	11.6	O _I	0.6155	0.0506	0.2668
	c	8.3680	θ'_M	13.0	O _{II}	0.2501	0.2150	0.0685
	α_{ac}	90.100	d/d'	1.117	O _{III}	0.8447	0.3149	-0.0568
	V	291.96						

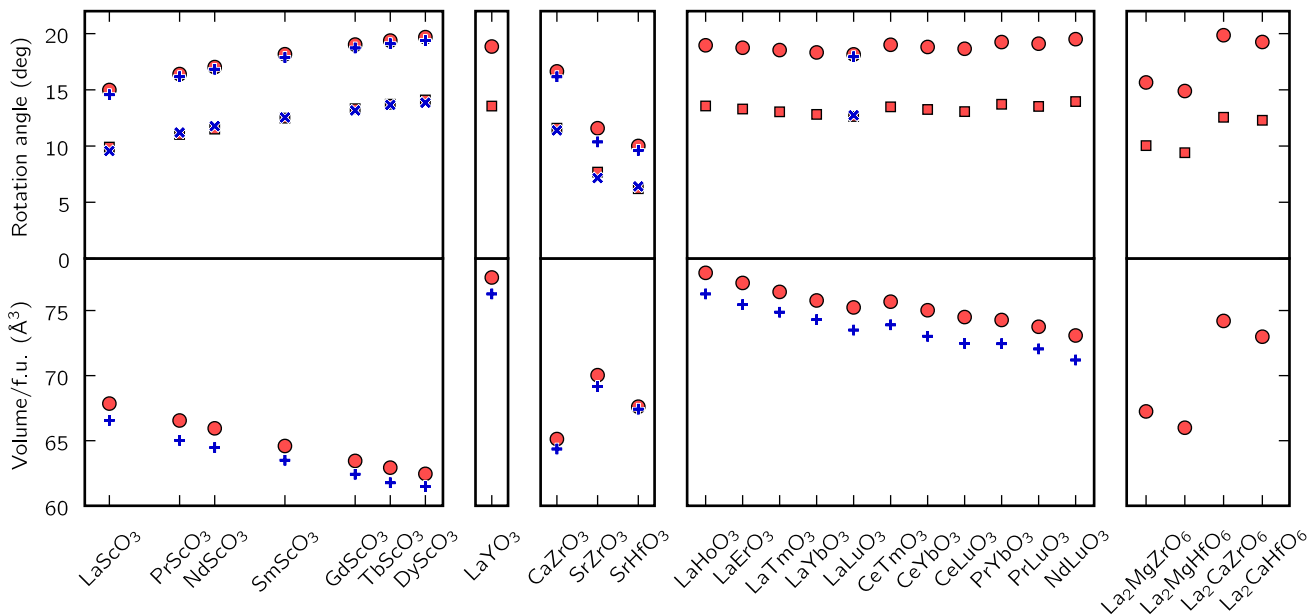


FIG. 5: Structural information for all systems we considered. Bottom pane shows volume in \AA^3 per formula unit (f. u.) of ABO_3 . Calculated values are shown as red circles, and experimental values as blue plus symbols, if available. Top pane shows oxygen octahedra rotation angles in degrees. Theoretical values are shown with red circles and squares and experimental values with blue plus and cross symbols. θ_R angles are shown with circles and plus symbols while θ_M angles with squares and cross symbols. For $\text{La}_2\text{BB}'\text{O}_6$ systems the average of θ_M and θ'_M is given. For numerical values see Table I and II.

orthorhombic and thus have diagonal dielectric tensors, with $\epsilon_{xx} \neq \epsilon_{yy} \neq \epsilon_{zz}$ in general. In addition to reporting these components, we also focus on analyzing the results in terms of the three linear combinations

$$\bar{\epsilon} = \frac{1}{3}(\epsilon_{xx} + \epsilon_{yy} + \epsilon_{zz}), \quad (13)$$

$$\Delta\epsilon_{\parallel} = \epsilon_{xx} - \epsilon_{yy}, \quad (14)$$

$$\Delta\epsilon_{\perp} = \epsilon_{zz} - \frac{1}{2}(\epsilon_{xx} + \epsilon_{yy}), \quad (15)$$

representing the average dielectric tensor, a measure of the x - y anisotropy, and a measure of z anisotropy, respectively. This choice of parameters was made to simplify the analysis of trends of dielectric properties of these compounds. The theoretical – and where available, experimental – results for the dielectric-tensor components are reported in Figure 7 and in Table III. The theoretical values are further decomposed in Table III into purely electronic or frozen-ion contributions ϵ^{el} and lattice-mediated contributions ϵ^{ion} . We find that the electronic contribution is roughly five times smaller than the ionic one, is nearly isotropic, and does not show a dramatic variation from one perovskite to another. Thus, it is clear that the lattice-mediated ionic contributions play by far the dominant role in the observed dielectric tensors and their anisotropies.

Our calculations of the zone-center phonon frequencies as well as the infrared activities for those modes that are infrared-active are given in the supplementary material.³³

We now consider each of our chosen classes of $Pbnm$ perovskites in turn, orienting the presentation from the point of view of the theoretical calculations, but mentioning the comparison with experiment where appropriate.

1. Rare-earth scandates

All rare-earth scandates $A\text{ScO}_3$ have rather similar values for their isotropically-averaged dielectric constants, falling between about $\bar{\epsilon} = 26$ and $\bar{\epsilon} = 28$. The xx component for all these systems is larger than the yy component by about $\Delta\epsilon_{\parallel} = 4$. On the other hand, the zz component changes significantly from LaScO_3 to DyScO_3 . In LaScO_3 the average of the xx and yy components is almost as large as the zz component ($\Delta\epsilon_{\perp} = -1$), while in DyScO_3 , the zz component is larger by about $\Delta\epsilon_{\perp} = 9$ than the average of xx and yy components.

These results are in good agreement with experiment, especially for $\bar{\epsilon}$ and $\Delta\epsilon_{\parallel}$. On the other hand, $\Delta\epsilon_{\perp}$ is consistently larger in experiments by about 3-5, but the trend of increasing $\Delta\epsilon_{\perp}$ is present in both theory and experiment.

As was mentioned earlier, rare-earth atoms heavier than Dy (i.e., Ho-Lu) and Y itself do not form single-crystal scandates. Nevertheless, at least some (YbScO_3 ³⁷ and LuScO_3 ²⁷) can form $Pbnm$ perovskites in thin-film form. In order to establish the trends of the dielectric

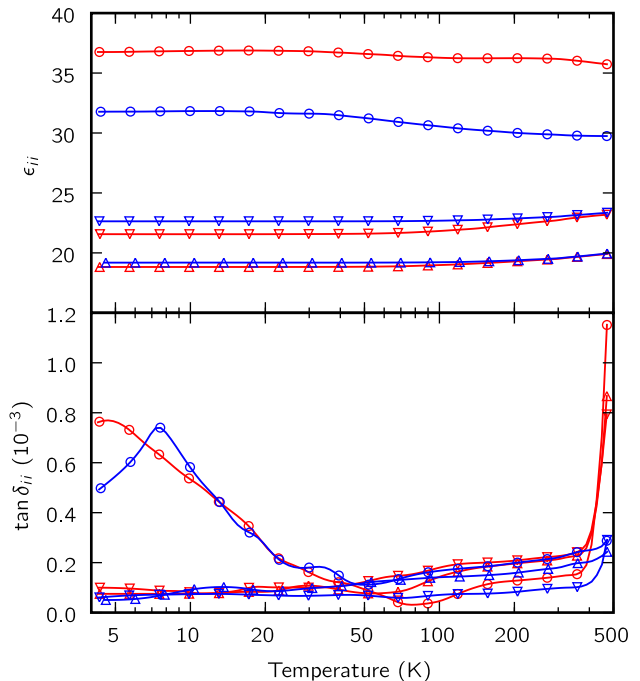


FIG. 6: Measured temperature dependence at 10 kHz of the dielectric tensor components (top panel) and dielectric loss (bottom panel) of GdScO_3 (blue) and DyScO_3 (red). Downward-pointing triangles denote ϵ_{xx} and $\tan \delta_{xx}$; upward-pointing triangles denote ϵ_{yy} and $\tan \delta_{yy}$; circles denote ϵ_{zz} and $\tan \delta_{zz}$.

properties for these materials, we calculated the dielectric tensors of LuScO_3 and YScO_3 . The dielectric tensor of LuScO_3 shows the continuation of the trend from LaScO_3 to DyScO_3 . Both xx and yy components are slightly smaller than for DyScO_3 , their numerical values being 23.5 and 21.4 respectively. On the other hand, the zz component (44.8) is larger than for DyScO_3 (32.6) and for LaScO_3 (27.4). YScO_3 has dielectric tensor components of 26.9, 23.0, and 37.7 for its xx , yy , and zz components, respectively.

The experimentally measured dependence of the dielectric tensor (and loss) components on temperature is shown in Fig. 6 for two compounds, GdScO_3 and DyScO_3 . In both cases we find that the dielectric tensor properties do not change significantly with temperature over the examined range (4.2-470 K). The ϵ_{zz} component slightly decreases with temperature while the ϵ_{xx} and ϵ_{yy} components show the opposite behavior. We expect that similar trends will be observed in all other rare-earth scandates.

As our calculated dielectric tensor is at 0 K and our measured dielectric tensor (Table III and IV) is at room temperature, the absence of a significant temperature dependence of the dielectric tensor is important to our ability to make a meaningful comparison between the calculated and measured coefficients.

Anomalies were observed in the dielectric loss along

the z axis ($\tan \delta_{zz}$) for both DyScO₃ and GdScO₃ below 50 K. The origin of these is unknown, but their presence suggests the possibility of a low-temperature phase transition.

2. Rare-earth yttrates

We now consider the rare-earth yttrates, i.e., AY₃O₃ where A is one of the rare-earth atoms. These are similar to the rare-earth scandates, but with yttrium on the B site instead of scandium. Only one such compound, LaYO₃, is known to form a perovskite,³⁸ but others might form in thin films via epitaxial stabilization. We find that LaYO₃ has a larger zz component than does LaScO₃. In LaYO₃ the zz component of the dielectric tensor is 38.0, while in LaScO₃ it is 27.4. On the other hand, the xx and yy components are almost unchanged with respect to LaScO₃. In LaYO₃ the xx component is 30.6 and the yy component is 25.7. We also find that heavier rare-earth atoms on the A -site tend to destabilize this $Pbnm$ structure even further. For example, we find that DyYO₃ in the $Pbnm$ structure has an unstable mode at $i70 \text{ cm}^{-1}$ that is IR-active along the z direction.

3. CaZrO₃, SrZrO₃, and SrHfO₃

According to our calculations, SrZrO₃ and SrHfO₃ show large and rather isotropic dielectric tensors. The average dielectric tensor $\bar{\epsilon}$ is 40.9 and 32.8 in SrZrO₃ and SrHfO₃, respectively. Their x - y anisotropies have an opposite sign as compared to all of the other compounds we analyzed. Unfortunately, because of twinning (see section II C 2), we could only measure an average dielectric constant for these systems, and therefore we could not directly compare our full calculated dielectric tensors with experiment. Still, if we make a comparison between theory and experiment for the average dielectric tensor $\bar{\epsilon}$, the agreement is reasonable.

Our calculations suggest that the CaZrO₃ compound, on the other hand, has a very high value of the z -anisotropy of 28.1. Its x - y anisotropy of 1.1, on the other hand, is quite small. The average dielectric tensor $\bar{\epsilon} = 43.6$ is the highest among the all compounds we considered, mostly because of the very large ϵ_{zz} component of the dielectric tensor. Very similar results were also obtained in other theoretical studies.^{68,69}

4. La₂BB'O₆ compounds

The La₂BB'O₆ systems show a small, non-zero off-diagonal ϵ_{xz} component, -0.4 for La₂MgZrO₃ and 4 for La₂CaZrO₃. ϵ_{xz} is allowed because the space group is reduced from orthorhombic ($Pbnm$) to monoclinic ($P2_1/c$) for these compounds. Their isotropically-averaged dielectric tensors are larger for systems containing Ca than for

those with Mg, and a bit larger for those with Zr than for those with Hf. Therefore, the dielectric response in this class of materials is largest for La₂CaZrO₆, with $\bar{\epsilon} = 28.5$, and smallest for La₂MgHfO₆, with $\bar{\epsilon} = 23.6$. All computed dielectric tensor components for these systems are given in Table IV.

5. Rare-earth rare-earth perovskites

The 11 rare-earth-rare-earth perovskites we considered show a bigger variation in the isotropically-averaged dielectric constant $\bar{\epsilon}$ than do the rare-earth scandates (LaScO₃ - DyScO₃). The largest average dielectric constant among them is 32.9 in LaHoO₃. The largest component of a dielectric tensor is also found in LaHoO₃, whose ϵ_{zz} is 41.7.

The measure $\Delta\epsilon_{\parallel}$ of x - y anisotropy shows little variation among the components in this series. The anisotropy is of the same sign as in the rare-earth scandates.

Finally, the z anisotropy $\Delta\epsilon_{\perp}$ once more shows a larger variation than in the rare-earth scandates. This anisotropy is largest for LaHoO₃ and smallest for LaLuO₃.

D. Decomposition of the ionic contribution to the dielectric tensor

As already mentioned, the ionic contribution to the dielectric tensor dominates in all of the systems we considered. The expression for the ionic contribution given in Eq. (4) provides a decomposition into contributions coming from eigenmodes of the force-constant matrix. The $Pbnm$ symmetry in perovskites, which is also approximately satisfied in La₂BB'O₆ compounds, allows a given eigenmode to contribute only to a single component (ϵ_{xx} , ϵ_{yy} , or ϵ_{zz}) of the dielectric tensor. This decomposition is given in Fig. 8 for all three components.

In rare-earth scandates, all three directions are evidently very different. The ϵ_{xx} component is dominated by a low-lying mode whose contribution is almost constant along the series (it contributes to ϵ_{xx} by 9.6 for LaScO₃ and 11.1 for DyScO₃). The ϵ_{yy} component, on the other hand, has sizable contributions coming from several modes. Finally, the ϵ_{zz} component comes mostly from a single low-lying mode. Unlike for the ϵ_{xx} component, the contribution from the mode responsible for the ϵ_{zz} component changes dramatically across the series, varying from 6.9 for LaScO₃ to 16.3 for DyScO₃. This explains the large value of the z anisotropy in DyScO₃ as compared to LaScO₃ that is visible in Fig. 7.

A behavior similar to that of the rare-earth scandates is also observed in LaYO₃ and in the rare-earth rare-earth perovskites. The SrZrO₃ and SrHfO₃ compounds show a quite similar behavior to each other. The ϵ_{xx} component has contributions coming from many modes, the ϵ_{yy} component is dominated by a single low-lying

TABLE III: Dielectric parameters of the perovskites with space group $Pbnm$ that we considered. Our calculated values are denoted by the letter T, our experimental values with E, and other theoretical data with O. First all three non-zero dielectric constant tensor components are given. Next, the average dielectric constant tensor, the x - y anisotropy, and z anisotropy are given; see Eqs. 13-15. Finally, the electronic and ionic contributions are given separately.

		Dielectric tensor			Reduced variables			Electronic part			Ionic part		
		ϵ_{xx}	ϵ_{yy}	ϵ_{zz}	$\bar{\epsilon}$	$\Delta\epsilon_{\parallel}$	$\Delta\epsilon_{\perp}$	$\epsilon_{xx}^{\text{el}}$	$\epsilon_{yy}^{\text{el}}$	$\epsilon_{zz}^{\text{el}}$	$\epsilon_{xx}^{\text{ion}}$	$\epsilon_{yy}^{\text{ion}}$	$\epsilon_{zz}^{\text{ion}}$
LaScO ₃	T	30.4	26.4	27.4	28.1	4.0	-1.0	5.0	5.0	4.8	25.3	21.5	22.6
PrScO ₃	T	28.6	24.2	26.2	26.3	4.4	-0.1	5.0	5.0	4.8	23.5	19.2	21.5
	E ^b	25.4	27.3	29.6	27.4	-1.9	3.3						
NdScO ₃	T	27.8	23.4	26.1	25.7	4.4	0.5	5.0	4.9	4.7	22.8	18.5	21.3
	E ^b	25.5	21.5	26.9	24.6	4.0	3.4						
SmScO ₃	T	27.2	22.9	27.3	25.8	4.3	2.3	4.9	4.9	4.7	22.2	18.0	22.7
	E ^b	23.1	19.9	29.0	24.0	3.2	7.5						
GdScO ₃	T	26.4	22.5	29.3	26.1	3.9	4.9	4.9	4.8	4.6	21.6	17.7	24.7
	E ^b	22.8	19.2	29.5	23.8	3.6	8.5						
TbScO ₃	T	26.1	22.4	30.7	26.4	3.7	6.5	4.8	4.8	4.6	21.2	17.6	26.1
DyScO ₃	T	25.7	22.3	32.6	26.9	3.5	8.6	4.8	4.8	4.5	20.9	17.5	28.0
	O ^a	24.1	21.2	27.7	24.3	2.9	5.1	4.9	4.9	4.7	19.2	16.3	23.0
	E ^b	21.9	18.9	33.8	24.9	3.0	13.4						
LaYO ₃	T	30.6	25.7	38.0	31.4	4.9	9.9	4.7	4.6	4.3	25.9	21.1	33.7
CaZrO ₃	T	34.8	33.7	62.4	43.6	1.1	28.1	4.6	4.7	4.6	30.2	29.1	57.8
	E ^f				30								
SrZrO ₃	T	38.0	41.5	43.3	40.9	-3.4	3.5	4.6	4.6	4.6	33.4	36.9	38.7
	O ^c	19.9	21.5	23.0	21.5	-1.6	2.3	5.1	4.9	4.8	14.8	16.6	18.2
	E ^b				32								
SrHfO ₃	T	30.0	35.1	33.2	32.8	-5.1	0.7	4.3	4.3	4.3	25.7	30.9	29.0
	O ^d	33.1	46.8	40.8	40.2	-13.7	0.9	4.4	4.3	4.3	28.7	42.4	36.5
	E ^b				26.2								
LaHoO ₃	T	31.0	26.0	41.7	32.9	5.0	13.3	4.7	4.6	4.3	26.3	21.4	37.4
LaErO ₃	T	29.9	25.0	36.4	30.4	4.9	9.0	4.7	4.6	4.3	25.2	20.4	32.1
LaTmO ₃	T	29.0	24.2	33.3	28.8	4.8	6.7	4.6	4.6	4.3	24.4	19.7	29.0
LaYbO ₃	T	28.3	23.6	30.9	27.6	4.7	5.0	4.6	4.5	4.3	23.6	19.1	26.6
LaLuO ₃ ^e	T	27.6	23.1	29.3	26.7	4.5	3.9	4.6	4.5	4.3	23.0	18.6	25.0
CeTmO ₃	T	27.9	23.5	34.9	28.8	4.4	9.2	4.6	4.6	4.3	23.3	18.9	30.6
CeYbO ₃	T	27.2	22.8	32.1	27.4	4.4	7.0	4.6	4.6	4.3	22.6	18.3	27.8
CeLuO ₃	T	26.6	22.3	30.2	26.4	4.3	5.7	4.6	4.5	4.3	22.0	17.8	25.9
PrYbO ₃	T	26.6	22.7	34.7	28.0	4.0	10.1	4.6	4.5	4.3	22.0	18.2	30.4
PrLuO ₃	T	26.1	22.0	32.2	26.8	4.0	8.1	4.6	4.5	4.3	21.5	17.5	27.9
NdLuO ₃	T	25.3	21.7	34.5	27.2	3.6	11.0	4.6	4.5	4.3	20.8	17.2	30.2

^aReference [30].

^bThis work.

^cReference [31].

^dReference [32].

^eExperimental data in reference [42].

^fReference [67].

TABLE IV: Dielectric parameters of the La₂BB'O₆ perovskites we considered. First all four dielectric constant tensor components are given, followed by the average value of the dielectric constant tensor. Finally, the electronic and ionic contributions to dielectric constant tensor are given. x axis is chosen along lattice vector a , y along b , and z close to c (with the small component along a due to monoclinic cell).

	Dielectric tensor					Electronic part				Ionic part			
	ϵ_{xx}	ϵ_{yy}	ϵ_{zz}	ϵ_{xz}	$\bar{\epsilon}$	$\epsilon_{xx}^{\text{el}}$	$\epsilon_{yy}^{\text{el}}$	$\epsilon_{zz}^{\text{el}}$	$\epsilon_{xz}^{\text{el}}$	$\epsilon_{xx}^{\text{ion}}$	$\epsilon_{yy}^{\text{ion}}$	$\epsilon_{zz}^{\text{ion}}$	$\epsilon_{xz}^{\text{ion}}$
La ₂ MgZrO ₆	26.5	23.6	24.4	-0.4	24.8	4.8	4.6	4.5	-0.06	21.7	18.9	19.8	-0.3
La ₂ MgHfO ₆	24.9	22.9	22.9	-0.3	23.6	4.6	4.5	4.4	-0.05	20.3	18.4	18.5	-0.3
La ₂ CaZrO ₆	29.9	24.9	30.6	3.8	28.5	4.7	4.6	4.4	-0.06	25.2	20.3	26.2	3.8
La ₂ CaHfO ₆	27.4	23.0	26.6	2.6	25.7	4.6	4.5	4.3	-0.04	22.9	18.5	22.3	2.6

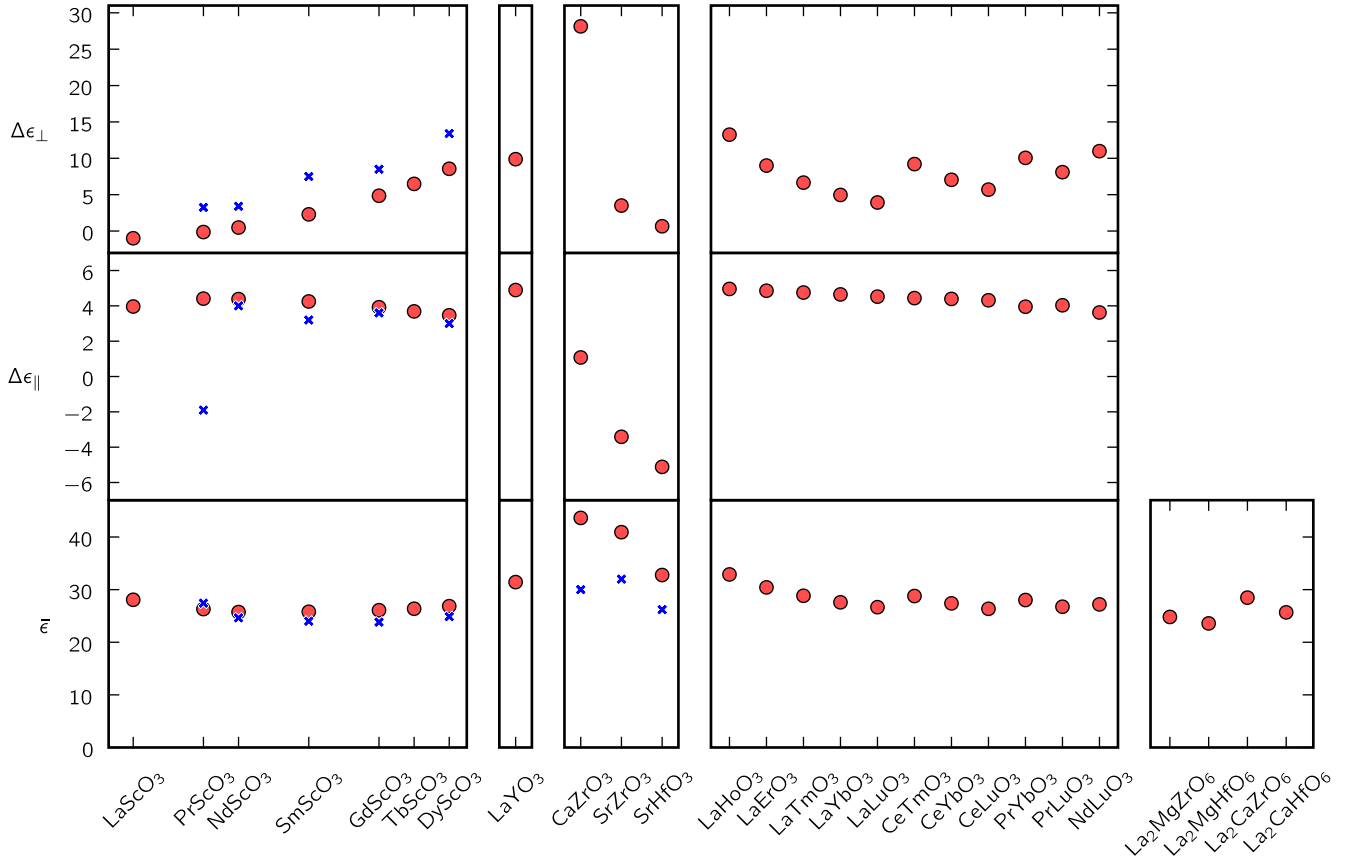


FIG. 7: Dielectric information for all systems we considered. Bottom pane shows average dielectric tensor $\bar{\epsilon}$, middle pane shows x - y anisotropy of the dielectric tensor, $\Delta\epsilon_{\parallel}$, and z anisotropy of the dielectric tensor $\Delta\epsilon_{\perp}$ is given in top pane. Calculated values are shown with red circles and experimental values with blue cross symbols, if available. See Table III for numerical values.

mode, and ϵ_{zz} is dominated by two low-lying modes. On the other hand, ϵ_{zz} component in CaZrO_3 shows very large contribution coming from a single low-lying mode. Finally, we note that the $\text{La}_2\text{BB}'\text{O}_6$ compounds containing Ca have stronger contributions to ϵ_{xx} and ϵ_{zz} from low-lying modes than do those containing Mg.

E. Compounds with $R\bar{3}c$ symmetry

At room temperature the ground state of BiFeO_3 is ferroelectric with polar space group $R\bar{3}c$, the pattern of octahedral rotations being $(a^-a^-a^-)$ in the Glazer notation. At higher temperature, however, BiFeO_3 undergoes a phase transition in which the ferroelectricity and the $(a^-a^-a^-)$ pattern of octahedral rotations disappear simultaneously.^{70,71} This observations led us to hypothesize that rotations of octahedra around the pseudocubic [111] axis, as in the $(a^-a^-a^-)$ pattern, tend to be energetically compatible with the presence of a ferroelectric distortion along the same axis. This would tend to suggest that perovskites that adopt the centrosymmetric $R\bar{3}c$ group, which also exhibits the $(a^-a^-a^-)$ pattern of oxygen octahedra, might be close to a ferroelectric insta-

bility leading to the lower-symmetry $R\bar{3}c$ space group, and thus that such compounds might have an especially large component of the dielectric tensor along the pseudocubic [111] axis.

To test this hypothesis, we have carried out a series of calculations on SrZrO_3 and GdScO_3 in which structural relaxation was allowed while maintaining the $R\bar{3}c$ symmetry. In both compounds we find some IR-active phonon modes that either have very low or imaginary frequency, indicating a near or actual instability. In the case of SrZrO_3 we find a mode that is active along the [111] pseudocubic direction and has an extremely small frequency of only 6 cm^{-1} , while for GdScO_3 we find that the corresponding mode is unstable with an imaginary frequency of $i142\text{ cm}^{-1}$. These calculations show that imposing the $R\bar{3}c$ structure on SrZrO_3 and GdScO_3 make them nearly or actually ferroelectric, thus confirming our hypothesis.

Incidentally, the observation that SrZrO_3 is more likely than GdScO_3 to be stabilized in the $R\bar{3}c$ structure is consistent with the fact that perovskite structures that prefer smaller rotation angles are more likely to form $R\bar{3}c$ than $Pbnm$ structures, as discussed by Woodward⁴⁴. We find that the rotational angles for SrZrO_3 in the $Pbnm$

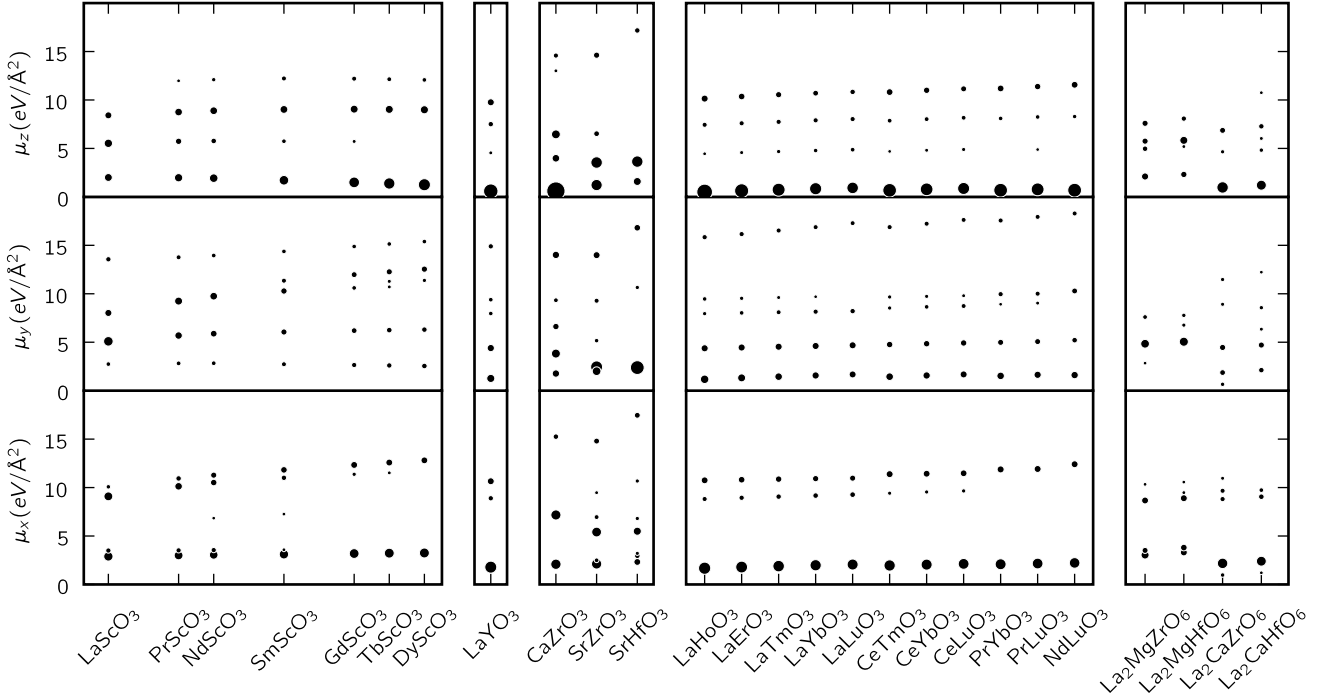


FIG. 8: Eigenvalues of a force constant matrix $\Phi_{i\alpha,j\beta}$ of modes that contribute to $\epsilon_{xx}^{\text{ion}}$ (first horizontal pane from bottom), $\epsilon_{yy}^{\text{ion}}$ (second pane), or $\epsilon_{zz}^{\text{ion}}$ (third) by more than 1.5. For each mode the area of the circle is proportional to its contribution to $\epsilon_{ii}^{\text{ion}}$. Eigenvalues are in $\text{eV}/\text{\AA}^2$.

space group are $\theta_R = 11.6^\circ$ and $\theta_M = 7.7^\circ$, while in GdScO_3 they are substantially larger, $\theta_R = 19.0^\circ$ and $\theta_M = 13.3^\circ$. More directly, we also find that the ground-state energy of SrZrO_3 having the $R\bar{3}c$ structure is only higher by 33.6 meV per formula unit than in the $Pbnm$ structure. On the other hand, in GdScO_3 the $R\bar{3}c$ is higher in energy by a much larger increment of 386 meV.

Finally, we note that LaAlO_3 , NdAlO_3 , and BaTbO_3 may also be of interest, as these all have the $R\bar{3}c$ space-group symmetry and should also be chemically stable on silicon.

F. Correlation between structural and dielectric properties

The heuristic observation about BiFeO_3 mentioned in the previous section (Sec. III E) led us to make a more detailed analysis of the correlation between structural and dielectric anisotropies in all five groups of $Pbnm$ perovskites. As can be seen from Fig. 3, the presence of the octahedral rotations breaks the symmetry among the three Cartesian directions in the $Pbnm$ perovskites. One would therefore naively expect that the anisotropy in the dielectric tensor component should also be correlated with the size of these rotation angles, but this is not what we observe. For example, LaScO_3 and DyScO_3 both have rather substantial octahedral rotation angles (θ_R is 14.9° in LaScO_3 and 19.7° in DyScO_3), but they have very different values of the dielectric z anisotropy

($\Delta\epsilon_\perp$ is -1.0 in LaScO_3 and 8.6 in DyScO_3). An even more extreme behavior can be seen in the case of rare-earth perovskites between, e.g., LaHoO_3 and LaLuO_3 .

Thus, we find no simple correlation between the dielectric tensor anisotropies and the values of the octahedral rotation angles. Instead, we find a correlation between the dielectric tensor anisotropies and the *mismatch* of the two rotation angles θ_R and θ_M , as we explain next.

While the $Pbnm$ symmetry does not impose any relationship between the two octahedral rotation angles θ_R and θ_M , we find in practice that all the compounds we studied obey the heuristic relationship $\theta_R \simeq \sqrt{2}\theta_M$. This means that the oxygen octahedra are rotated about the three Cartesian axes by almost the same rotation angle, or equivalently, that the rotation axis is nearly $\langle 111 \rangle$. In the Glazer language, these $Pbnm$ perovskites having $(a^-a^-c^+)$ rotations can be said to be very close to an $(a^-a^-a^+)$ pattern. We can measure the mismatch between the actual $(a^-a^-a^+)$ and the hypothetical $(a^-a^-c^+)$ rotation pattern by the quantity $\theta_M - \theta_R/\sqrt{2}$, and it is this quantity that we find to be strongly correlated with the dielectric anisotropy $\Delta\epsilon_\perp$.

This is shown in Fig. 9, where $\Delta\epsilon_\perp$ is plotted versus $\theta_M - \theta_R/\sqrt{2}$ for all of the compounds considered in this work. It is apparent that the III-III-valent perovskites have a different behavior than the II-IV-valent ones. Nevertheless, we conclude that in both cases there is a strong correlation between the mismatch angle and the dielectric tensor anisotropy. The sign of the correla-

tion is such that a deviation from the $(a^-a^-a^+)$ pattern having an increased rotation angle around the z axis gives a larger dielectric tensor component along the z axis, and thus a larger z anisotropy $\Delta\epsilon_{\perp}$.

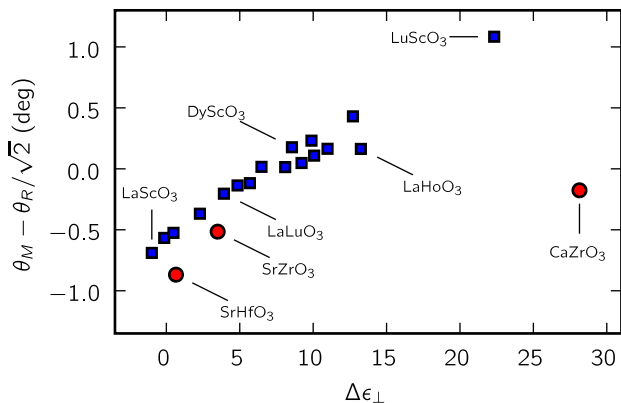


FIG. 9: Correlation between the dielectric tensor z -anisotropy ($\Delta\epsilon_{\perp}$) and the mismatch in the oxygen octahedra rotation angle. Only some perovskites are labeled. Perovskites where both A and B ions are III-valent are indicated with blue square symbols and those where A ions are II-valent and B are IV-valent are indicated with red circles.

G. Antisite substitutions

Experimentally the compositions of the perovskites that we have been describing up to now by their nominal compositions, e.g., LaLuO_3 , are in fact slightly different from the compositions of the single crystals on which the dielectric tensors were measured. This is because our crystals are grown at the congruently melting compositions, e.g., $\text{La}_{0.94}\text{Lu}_{1.06}\text{O}_3$, which differ from the nominal compositions described up to now. The congruently melting compositions of all relevant $Pbnm$ perovskites studied have been found to be poor in the A -site cation and rich in the B -site cation composition.^{59,72,73}

For this reason, we decided to carry out a theoretical analysis of the effects of B atoms substituting at the A site on the structural and dielectric properties of the material. Detailed calculations were done only for the case of LaLuO_3 , but we expect that similar trends will be observed in the remaining rare-earth rare-earth perovskites as well as in the rare-earth scandates and yttrates. Of course, other kinds of compositional disorder might also be present, but such possibilities are not analyzed here.

1. Analysis of antisite defects in LaLuO_3

We studied Lu_{La} antisite defects in LaLuO_3 using a supercell approach. Specifically, in order to model a situation in which one of every 16 La atoms is substituted

by Lu, which is about a 6% substitution, we constructed an 80-atom supercell containing a single antisite defect. The supercell is enlarged with respect to the primitive 20-atom $Pbnm$ primitive cell by doubling along both the orthorhombic a and b lattice vectors. The resulting stoichiometry is

$$(\text{La}_{0.9375}\text{Lu}_{0.0625})\text{LuO}_3 \quad \text{or} \quad \text{La}_{0.9375}\text{Lu}_{1.0625}\text{O}_3.$$

The presence of the Lu_{La} antisite in this particular 80-atom supercell reduces the crystal symmetry from orthorhombic $Pbnm$ to monoclinic Pm . After full relaxation of the crystal structure in this space group, we find that the a , b , and c lattice vectors are reduced by 0.3%, 0.2%, and 0.1%, respectively, while the monoclinic angle between a and b lattice vectors of 90.03° deviates only very slightly from 90° .

The influence of the Lu_{La} substitution on the dielectric properties is more complex. Evaluated in the same coordinate frame as in the $Pbnm$ unit cell, the ϵ_{xx} and ϵ_{yy} dielectric tensor components remain almost unchanged, and the new ϵ_{xy} component allowed by the monoclinic symmetry is quite small, only 2.1. On the other hand, the ϵ_{zz} component is drastically altered by the presence of Lu atom on the La site. In fact, we find that the 80-atom supercell is actually just barely unstable in the Pm space group, as indicated by the presence of a phonon mode with a very small imaginary frequency of $i16 \text{ cm}^{-1}$.⁷⁴ The contribution of this phonon mode to the ϵ_{zz} component (evaluated in the unstable Pm structure) is therefore negative, specifically, -33.6 . Since this phonon frequency is so close to zero, we expect that it would get renormalized to positive frequency at room temperature. For this reason, we did not follow the structural relaxation of our 80-atom supercell along the direction of the unstable mode, and a realistic estimate of the dielectric response of the system is difficult. Nevertheless, we conclude that Lu_{La} substitutions in LaLuO_3 have the potential to increase the ϵ_{zz} dielectric tensor component substantially.

2. Discussion

As can be clearly seen in Fig. 7, our calculated z anisotropy ($\Delta\epsilon_{\perp}$) is consistently larger than the measured one for all the rare-earth scandates for which we have experimental measurements. In view of the calculations reported for LaLuO_3 above, we tentatively attribute this discrepancy to the generic tendency of B atoms to substitute on the A site in these compounds. This observation is consistent with the fact that smaller B ions that substitute for larger A ions will reside in a relatively larger cage, providing room to rattle and thereby contribute to an enhanced dielectric response.

IV. SUMMARY

The main focus of this work has been the application of both computational and experimental methods to study the structural and dielectric properties of various $Pbnm$ perovskites that have potentially large dielectric tensor components and are chemically stable on silicon up to ~ 1000 °C.² Such compounds might be good candidates for future use as high- K dielectrics in microelectronics applications, e.g., as a possible replacement of hafnia-based high- K dielectrics currently used in the CMOS transistors in integrated circuits.

Of the compounds we have considered, CaZrO_3 , SrZrO_3 , LaHoO_3 , and LaYO_3 appear to be especially promising. CaZrO_3 has the largest calculated average dielectric tensor ($\bar{\epsilon} = 43.6$) among the compounds we considered, and SrZrO_3 is a close second with $\bar{\epsilon} = 40.9$. The dielectric tensor in CaZrO_3 is very anisotropic, with its ϵ_{zz} component almost twice as large as ϵ_{xx} or ϵ_{yy} , while on the other hand SrZrO_3 has an almost isotropic dielectric tensor. Unfortunately, the full dielectric tensors of these compounds have not yet been measured due to lack of single crystals.

Of the rare-earth rare-earth $Pbnm$ perovskites, only LaLuO_3 has had its dielectric tensor measured to date. Our results on this compound will be presented in detail elsewhere.⁴² The theoretical calculations, however, indicate that other compounds in this series should have even larger dielectric tensor components, with LaHoO_3 , having $\bar{\epsilon} = 32.9$, being the most promising among these. LaYO_3 is expected to behave very similar to LaHoO_3 since Y and Ho have almost the same ionic radii, so it may be promising as well ($\bar{\epsilon} = 31.4$). Thus, this series of compounds clearly deserves additional scrutiny.

Of course, there are good reasons for preferring amorphous over single-crystalline materials for such high- K applications. Certainly the ability of amorphous SiO_2

to conform to the substrate and to eliminate electrical traps played a central role in its dominance as the gate dielectric of choice for 40 years for silicon-based metal-oxide-semiconductor field-effect transistors. The present hafnia-based high- K dielectrics are amorphous or nanocrystalline.⁷⁵ For this reason, any eventual application of these materials for high- K applications would presumably require the adoption of one of two strategies. The first is the possibility of growing crystalline epitaxial oxides directly on silicon, which clearly would require a very high level of control of interface chemistry and morphology before it could become a practical solution. The second is the possibility that some of the compounds investigated here could be synthesized in amorphous or nanocrystalline form. We have not investigated these issues here, nor have we tried to calculate what (possibly very substantial) changes in the dielectric properties would occur in the amorphous counterparts, as this would take us far beyond the scope of the present study. Nevertheless, these are important questions for future investigations.

Acknowledgments

The work of S. C. and D. V. was supported in part by NSF Grant DMR-0545198. The work of T.H. was supported by the Pennsylvania State University Materials Research Institute Nanofabrication Lab, the National Science Foundation Cooperative Agreement No. 0335765 and National Nanotechnology Infrastructure Network, with Cornell University. S. T. M. acknowledge support from NSF DMR-0602770. The research conducted by M. D. B. at the Center for Nanophase Materials Sciences, is sponsored at Oak Ridge National Laboratory by the Division of Scientific User Facilities, U.S. Department of Energy. D. G. S. would like to acknowledge support from the Semiconductor Research Corporation and Intel.

* Electronic address: sinisa@physics.rutgers.edu

† Deceased.

¹ G. Moore, in *2003 IEEE International Solid-State Circuits Conference*. (Piscataway, NJ, USA, 2003), vol. 1, pp. 20–23.

² D. G. Schlom, C. A. Billman, J. H. Haeni, J. Lettieri, P. H. Tan, R. R. M. Held, S. Völkl, and K. J. Hubbard, in *Thin Films and Heterostructures for Oxide Electronics*, edited by S. B. Ogale (Springer, 2005), pp. 31–78.

³ D. G. Schlom, S. Guha, and S. Datta, *Mater. Res. Bull.* **33**, 1017 (2008).

⁴ J. Robertson, *J. Appl. Phys.* **104**, 124111 (2008).

⁵ K. Mistry, C. Allen, C. Auth, B. Beattie, D. Bergstrom, M. Bost, M. Brazier, M. Buehler, A. Cappellani, R. Chau, et al., in *Electron Devices Meeting, 2007. IEDM 2007. IEEE International* (2007), pp. 247–250.

⁶ J. Hicks, D. Bergstrom, M. Hattendorf, J. Jopling, J. Maiz, S. Pae, C. Prasad, and J. Wiedemer, *Intel Technol. J.* **12**, 131 (2008).

⁷ D. Scansen, *Under the hood: 45 nm: What intel didn't tell you* (21 Jan. 2008), www.techonline.com/product/underthehood/205918004.

⁸ S. Guha and V. Narayanan, *Phys. Rev. Lett.* **98**, 196101 (2007).

⁹ H. M. Christen, J. G. E. Jellison, I. Ohkubo, S. Huang, M. E. Reeves, E. Cicerrella, J. L. Freeouf, Y. Jia, and D. G. Schlom, *Appl. Phys. Lett.* **88**, 262906 (2006).

¹⁰ V. V. Afanas'ev, A. Stesmans, C. Zhao, M. Caymax, T. Heeg, J. Schubert, Y. Jia, D. G. Schlom, and G. Lucovsky, *Appl. Phys. Lett.* **85**, 5917 (2004).

¹¹ C. Zhao, T. Witters, B. Brijs, H. Bender, O. Richard, M. Caymax, T. Heeg, J. Schubert, V. V. Afanas'ev, A. Stesmans, et al., *Appl. Phys. Lett.* **86**, 132903 (2005).

¹² T. Heeg, J. Schubert, C. Buchal, E. Cicerrella, J. Freeouf, W. Tian, Y. Jia, and D. Schlom, *Appl. Phys. A* **83**, 103 (2006).

¹³ L. Edge, D. Schlom, S. Stemmer, G. Lucovsky, and J. Lun- ing, *Radiat. Phys. Chem.* **75**, 1608 (2006).

- ¹⁴ E. Cicerrella, J. L. Freeouf, L. F. Edge, D. G. Schlom, T. Heeg, J. Schubert, and S. A. Chambers, *J. Vac. Sci. Technol., A* **23**, 1676 (2005).
- ¹⁵ V. V. Afanas'ev, A. Stesmans, L. F. Edge, D. G. Schlom, T. Heeg, and J. Schubert, *Appl. Phys. Lett.* **88**, 032104 (2006).
- ¹⁶ L. F. Edge, D. G. Schlom, S. Rivillon, Y. J. Chabal, M. P. Agustin, S. Stemmer, T. Lee, M. J. Kim, H. S. Craft, J.-P. Maria, et al., *Appl. Phys. Lett.* **89**, 062902 (2006).
- ¹⁷ P. Sivasubramani, T. H. Lee, M. J. Kim, J. Kim, B. E. Gnade, R. M. Wallace, L. F. Edge, D. G. Schlom, F. A. Stevie, R. Garcia, et al., *Appl. Phys. Lett.* **89**, 242907 (2006).
- ¹⁸ J. Lopes, M. Roeckerath, T. Heeg, U. Littmark, J. Schubert, S. Mantl, Y. Jia, and D. Schlom, *Microelectron. Eng.* **84**, 1890 (2007).
- ¹⁹ M. Wang, W. He, T. P. Ma, L. F. Edge, and D. G. Schlom, *Appl. Phys. Lett.* **90**, 053502 (2007).
- ²⁰ L. Edge, W. Tian, V. Vaithyanathan, T. Heeg, D. Schlom, D. Klenov, S. Stemmer, J. Wang, and M. Kim, in *ECS Trans.* (Honolulu, HI, United states, 2008), vol. 16, pp. 213 – 227.
- ²¹ E. D. Özben, J. M. J. Lopes, M. Roeckerath, S. Lenk, B. Holländer, Y. Jia, D. G. Schlom, J. Schubert, and S. Mantl, *Appl. Phys. Lett.* **93**, 052902 (2008).
- ²² M. Roeckerath, J. Lopes, E. Durgun Ozben, C. Sandow, S. Lenk, T. Heeg, J. Schubert, and S. Mantl, *Appl. Phys. A* **94**, 521 (2009).
- ²³ M. Wagner, T. Heeg, J. Schubert, C. Zhao, O. Richard, M. Caymax, V. Afanas'ev, and S. Mantl, *Solid-State Electron.* **50**, 58 (2006).
- ²⁴ P. Myllymaki, M. Roeckerath, M. Putkonen, S. Lenk, J. Schubert, L. Niinisto, and S. Mantl, *Appl. Phys. A* **A88**, 633 (Sept. 2007).
- ²⁵ K. H. Kim, D. B. Farmer, J.-S. M. Lehn, P. V. Rao, and R. G. Gordon, *Appl. Phys. Lett.* **89**, 133512 (2006).
- ²⁶ R. Thomas, P. Ehrhart, M. Roeckerath, S. van Elshocht, E. Rijs, M. Luysberg, M. Boese, J. Schubert, M. Caymax, and R. Waser, *J. Electrochem. Soc.* **154**, 147 (2007).
- ²⁷ T. Heeg, M. Roeckerath, J. Schubert, W. Zander, C. Buchal, H. Y. Chen, C. L. Jia, Y. Jia, C. Adamo, and D. G. Schlom, *Appl. Phys. Lett.* **90**, 192901 (2007).
- ²⁸ W. Wersing, *Curr. Opin. Solid State Mater. Sci.* **1**, 715 (1996).
- ²⁹ T. A. Vanderah, *Science* **298**, 1182 (2002).
- ³⁰ P. Delugas, V. Fiorentini, A. Filippetti, and G. Pourtois, *Phys. Rev. B* **75**, 115126 (2007).
- ³¹ R. Vali, *Solid State Commun.* **145**, 497 (2008).
- ³² R. Vali, *Solid State Commun.* **149**, 519 (2009).
- ³³ See www.physics.rutgers.edu/~sinisa/highk/supp.pdf or <http://link.aps.org/supplemental/10.1103/PhysRevB.82.064107> for zone-center phonon frequencies, as well as the infrared activities for those modes that are infrared-active.
- ³⁴ J. Badie, *Rev. Int. Hautes Temp. Réfact., Fr* **15**, 183 (1978).
- ³⁵ J. Badie and M. Foex, *J. Solid State Chem.* **26**, 311 (1978).
- ³⁶ J.-P. Coutures, J. Badie, R. Berjoan, J. Coutures, R. Flaman, and A. Rouanet, *High Temp. Sci.* **13**, 331 (1980).
- ³⁷ J. Schubert (private communication).
- ³⁸ U. Berndt, D. Maier, and C. Keller, *J. Solid State Chem.* **13**, 131 (1975).
- ³⁹ A. Rabenau, *Z. Anorg. Allg. Chem.* **288**, 221 (1956).
- ⁴⁰ K. Ito, K. Tezuka, and Y. Hinatsu, *J. Solid State Chem.* **157**, 173 (2001).
- ⁴¹ M. Bharathy, A. Fox, S. Mugavero, and H.-C. zur Loye, *Solid State Sci.* **11**, 651 (2009).
- ⁴² T. Heeg, K. Wiedenmann, M. Roeckerath, S. Coh, D. Vanderbilt, J. Schubert and D. G. Schlom, unpublished.
- ⁴³ V. Goldschmidt, *Naturwissenschaften* **21**, 477 (1926).
- ⁴⁴ P. M. Woodward, *Acta Crystallogr. Sect. B* **53**, 32 (1997).
- ⁴⁵ A. M. Glazer, *Acta Crystallogr. Sect. B* **28**, 3384 (1972).
- ⁴⁶ P. Giannozzi, S. Baroni, N. Bonini, M. Calandra, R. Car, C. Cavazzoni, D. Ceresoli, G. L. Chiarotti, M. Cococcioni, I. Dabo, et al., *Journal of Physics: Condensed Matter* **21**, 395502 (19pp) (2009), URL <http://www.quantum-espresso.org>.
- ⁴⁷ J. P. Perdew, K. Burke, and M. Ernzerhof, *Phys. Rev. Lett.* **77**, 3865 (1996).
- ⁴⁸ D. Vanderbilt, *Phys. Rev. B* **32**, 8412 (1985).
- ⁴⁹ H. J. Monkhorst and J. D. Pack, *Phys. Rev. B* **13**, 5188 (1976).
- ⁵⁰ V. N. Staroverov, G. E. Scuseria, J. Tao, and J. P. Perdew, *Phys. Rev. B* **69**, 075102 (2004).
- ⁵¹ W. Pies and A. Weiss, *Landolt-Börnstein - Group III Condensed Matter* (Springer-Verlag, 2006), vol. 7c1, chap. VI.1.5.1, pp. 14–34.
- ⁵² In the case of GdN the anomaly is more likely the result of the large spin splitting and strong ferromagnetism associated with the huge magnetic moment of the $4f^7$ configuration.
- ⁵³ S. Baroni, S. de Gironcoli, A. Dal Corso, and P. Giannozzi, *Rev. Mod. Phys.* **73**, 515 (2001).
- ⁵⁴ E. Cockayne and B. P. Burton, *Phys. Rev. B* **62**, 3735 (2000).
- ⁵⁵ R. Uecker, H. Wilke, D. Schlom, B. Velickov, P. Reiche, A. Polity, M. Bernhagen, and M. Rossberg, *J. Cryst. Growth* **295**, 84 (2006).
- ⁵⁶ R. Uecker, B. Velickov, D. Klimm, R. Bertram, M. Bernhagen, M. Rabe, M. Albrecht, R. Fornari, and D. Schlom, *J. Cryst. Growth* **310**, 2649 (2008).
- ⁵⁷ The SrZrO₃, SrHfO₃, and LaScO₃ single crystals were grown by float-zone by Dima Souptel and Anatoly Balbashov of the Moscow Power Engineering Institute, Moscow, Russia. For details on the growth parameters see D. Souptel, G. Behr, and A.M. Balbashov, *J. Cryst. Growth* **236**, 583 (2002).
- ⁵⁸ R. Newnham, *Properties of Materials: Anisotropy, Symmetry, Structure* (Oxford University Press, Oxford, 2005).
- ⁵⁹ T. M. Gesing, R. Uecker, and J.-C. Buhl, *Z. Kristallogr. NCS* **224**, 365 (2009).
- ⁶⁰ M. T. Anderson, K. B. Greenwood, G. A. Taylor, and K. R. Poeppelmeier, *Prog. Sol. St. Chem.* **22**, 197 (1993).
- ⁶¹ R. P. Liferovich and R. H. Mitchell, *J. Phys. Chem. Solids* **177**, 2188 (2004).
- ⁶² B. Velickov, V. Kahlenberg, R. Bertram, and M. Bernhagen, *Z. Kristallogr.* **9**, 466 (2007).
- ⁶³ B. J. Kennedy, C. J. Howard, and B. C. Chakoumakos, *Phys. Rev. B* **59**, 4023 (1999).
- ⁶⁴ B. J. Kennedy, C. J. Howard, and B. C. Chakoumakos, *Phys. Rev. B* **60**, 2972 (1999).
- ⁶⁵ B. Velickov, V. Kahlenberg, R. Bertram, and R. Uecker, *Acta Crystallogr. Sect. E* **64**, i79 (2008).
- ⁶⁶ E. Ruiz-Trejo, M. S. Islam, and J. A. Kilner, *Solid State Ionics* **123**, 121 (1999).
- ⁶⁷ I. Levin, T. G. Amos, S. M. Bell, L. Farber, T. A. Vanderah, R. S. Roth, and B. H. Toby, *J. Solid State Chem.* **175**, 170 (2003), ISSN 0022-4596.
- ⁶⁸ J. W. Bennett, private communication.

- ⁶⁹ J. W. Bennett, I. Grinberg, and A. M. Rappe, *Chem. Mater* **20**, 5134 (2008).
- ⁷⁰ D. C. Arnold, K. S. Knight, F. D. Morrison, and P. Lightfoot, *Phys. Rev. Lett.* **102**, 027602 (2009).
- ⁷¹ R. Haumont, I. A. Kornev, S. Lisenkov, L. Bellaiche, J. Kreisel, and B. Dkhil, *Phys. Rev. B* **78**, 134108 (2008).
- ⁷² G. W. Berkstresser, A. J. Valentino, and C. D. Brandle, *J. Cryst. Growth* **128**, 684 (1993).
- ⁷³ K. L. Ovanesyan, A. Petrosyan, G. O. Shirinyan, C. Pedrini, and L. Zhang, *J. Cryst. Growth* **198**, 497 (1999).
- ⁷⁴ The eigendisplacement of this unstable mode is very close to that of the S -point $(\frac{1}{2}\frac{1}{2}0)$ phonon of the 20-atom $Pbnm$ structure having a frequency of 39 cm^{-1} . However, this phonon remains inactive in the $Pbnm$ structure because it does not appear at the Γ point.
- ⁷⁵ D. A. Muller, private communication.